

## Development of FeCu<sub>x</sub>/FeS/Graphite Composite Electrode Materials for Iron-Based Alkaline Batteries

Tendai Tawonezvi<sup>1,2,\*</sup>, Bernard Jan Bladergroen<sup>1</sup>, Joe John<sup>2</sup>

<sup>1</sup> South African Institute for Advanced Materials Chemistry (SAIAMC), University of the Western Cape, Robert Sobukwe Road, Bellville, Cape Town, 7535, South Africa

<sup>2</sup> Department of Chemical Engineering, Cape Peninsula University of Technology, Symphony Way, Bellville, Cape Town, 7535, South Africa

\*E-mail: [tendaitawonezvi@yahoo.com](mailto:tendaitawonezvi@yahoo.com)

Received: 20 January 2020 / Accepted: 30 September 2020 / Published: 31 October 2020

In an attempt to enhance the electrochemical performance of the iron-based electrode, an iron-core copper-shell nano-structured material was synthesized and incorporated with ferrous sulphide, and graphite additives. An electrically conductive nickel mesh as a current collector, coupled with a low-cost hot-pressing technique, was employed to formulate the electrodes. The ferrous and graphite integrated iron-core copper-shell nano-structured negative electrode was investigated for applications in Fe-based alkaline batteries energy storage. FeCu<sub>0.25</sub>/15%FeS/5%C composite electrode delivered a specific discharge capacity of 385 mAh g<sup>-1</sup> an approximately 71% coulombic efficiency. The nominal specific capacity of the electrode exhibited negligible capacity degradation after 40 cycles. Ex-situ X-ray Diffraction characterisations and scanning electrode microscopy images of both the fresh and the discharged electrode surfaces show that particle arrangement was still intact after 40 cycles, with negligible particle agglomeration compared to the pure iron electrode surface which was marked with massive agglomeration. Energy filtered transmission electrode microscopy images confirmed the iron-core copper-shell particle arrangement. The FeCu<sub>0.25</sub>/15%FeS/5%C electrode exhibited stable performances marked by high specific capacity coupled with negligible capacity decay and high efficiency. The ferrous/graphite integrated iron-core copper-shell electrode is consequently a conducive negative electrode candidate in alkaline iron-air and nickel-iron battery systems.

**Keywords:** Energy Storage, Iron-based Alkaline Battery, Iron-Core Copper-Shell, Composite Iron-Copper/Sulphide Electrode

### 1. INTRODUCTION

The world economy currently relies eminently on non-renewable energy sources such as coal, oil, metal ores and natural gas [1]. The mounting utilisation of these dwindling resources owing to

rampant economic development and exponential population growth is becoming critically unsustainable and this has fuelled the development of sustainable alternative energy sources.

In the past few years, renewable energy sources, such as the wind, water and solar resources, have emanated as the ideal and suitable energy sources to boost energy security and supply, and alleviate ecological and environmental matters [1–4]. Renewable energy sources have the potential to significantly lower greenhouse gas emissions while offering a practical mode to reduce, or possibly eliminate fossil fuel dependency, this is mainly due to their eco-friendly nature and absolute abundance. It is thus apparent why most countries are taking drastic steps to implement economic policies that will accelerate the utilisation of such clean resources [1,5,6]. As a result, renewable energy-based power generation plants have emerged as the fastest-growing power production plants [2,7]. Global wind and solar power production exceeded 1100 GW in 2018, an increase of a staggering 680% compared to the previous 10 years [1].

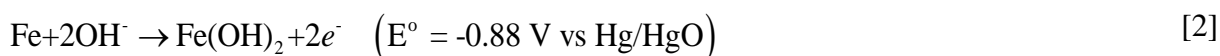
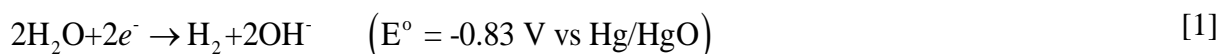
However, generation of energy from renewable resources (wind, solar etc) is not always feasible when the energy demand peaks (stochastic wind profiles and seasonal availability of sunlight, water and wind resources). The integration of renewable energy generation and energy storage, therefore, fosters a transcendent key to the drift between the sporadic energy generation trend from renewable energy sources and energy demand.

Electrochemical energy storage offers an ideal viable solution that would instil stability in the electrical energy grid by mitigating the intermittent energy generation trend from renewable energy sources to match energy demand. This solution is pragmatic mostly due to its high round-trip efficiency, long cycle life, low cost, and scalability compared to other energy storage technologies [1,3,5,6]. Only a few of the several battery technologies developed in the last century have been demonstrated in large-scale applications. Among the various developed battery technologies, aqueous batteries have the potential to help stabilise the future electrical energy grid at a lower cost than any of their non-aqueous counterparts (such as Na-ion, Zn-ion, Li-ion, etc.). This is attributed to their utilisation of low-cost water-based electrolyte and abundant raw materials. In addition, non-aqueous batteries require integration of costly safety systems to minimise the risk of fire and explosions; such costly systems are inessential for aqueous batteries [5,7].

Lead-acid (Pb-acid) batteries are the oldest, most commercially deployed aqueous energy storage technology; however, its energy density ( $\sim 35\text{--}40 \text{ Wh kg}^{-1}$ ), the toxicity of raw materials, and short cycle life hinder its potential as an ideal renewable energy storage technology candidate [3,5,6]. In contrast, nickel-iron (Ni-Fe) batteries, invented and commercially deployed in the early 20th century, could potentially deliver double to triple the specific energy capacity of Pb-acid batteries. Ni-Fe also offers increased robustness and longer cycle life at a deep discharge state (>10000 cycles at 75% Depth of Discharge) [8]. In addition, with Ni-Fe batteries exceeding 10000 cycles of charge and discharge, they significantly surpass most of their competing energy storage technology counterparts, such as is Pb-acid (300–400 cycles), nickel-metal hydride (500–800) and nickel-cadmium (1300–1600 cycles) [3,5,8].

The revived interest in the Fe-based alkaline batteries (such as Ni-Fe and Fe-Air), has been largely propelled by the incentive to develop efficient, robust and low-cost storage technologies. Ni-Fe alkaline batteries are secondary batteries that are robust, non-toxic, and eco-friendly [2,9]. Ni-Fe batteries could foster a cost-effective solution to store energy for grid system applications due to the

relative abundance of raw materials required to build the technology. However, the successful commercial deployment of this battery technology has been diminished by their poor coulombic efficiency (40–60%), low discharge rate capability and relatively poor specific energy (~50 Wh kg<sup>-1</sup>) [10]. The poor coulombic efficiency is a direct result of the parasitic evolution of hydrogen gas during charging of the Fe-based electrode, while the low discharge capability results from passivation of the Fe-based electrode, attributed to an insulating layer of the less reactive iron hydroxide (Fe(OH)<sub>2</sub>) generated during the discharge process [10,11]. The parasitic evolution of hydrogen is due to the standard reduction potential of the hydrogen reaction (Equation 1) being more positive than the Fe electrode electrochemical reaction (Equation 2.)



The Fe-based electrode exhibits a prominent influence (compared to other components) on the overall electrochemical performance of the battery; therefore, by altering the electrode material composition, design, nanostructure and/or production techniques, the battery's overall electrochemical performance will subsequently improve [11]. To suppress the hydrogen evolution reaction and increase specific capacity, various sulphide and carbon components have been added as electrode- or electrolyte-additives. Among them, Bi<sub>2</sub>O<sub>3</sub>, Bi<sub>2</sub>S<sub>3</sub>, FeS and organo-sulphurs are considered as the most effective [6,11–14]. Most of the compounds form different iron sulphide phases, while elemental bismuth metal is formed during charging, consequently increasing the overpotential for hydrogen evolution [14,15]. Nanoparticles have proved beneficial for enhancing the utilization of the Fe active materials [16,17]; Synthesized nano Fe-core Cu-shell composite electrode material, with a high concentration of Cu, could discharge up to 150 mAh g<sup>-1</sup> at a current density of 2000 mA g<sup>-1</sup> [10].

In this study, a combination of both Cu and FeS additives plus graphite particles is used. FeS/C substituted Fe-Cu composite material was synthesized as anode material to be utilised in Fe-based alkaline batteries. The rationale behind this is that Cu should circumvent Fe particle agglomeration during cycling, graphite should formulate a good conductive network, subsequently improving the reversibility of the active material, and FeS should impede the parasitic hydrogen evolution reaction and the passivation process.

## 2. MATERIAL AND METHODS

### 2.1. Materials

The reagents Fe (Hoganas, Sweden), FeS (Sigma Aldrich, USA), Graphite (Alfa Aesar, United States), Coateylene HA16 (AXALTA, United States), potassium hydroxide (KOH) (99%) (Sigma Aldrich, USA), lithium hydroxide (LiOH) (98%) (Sigma Aldrich, USA) and nickel mesh (Q-Lite batteries, China) were purchased were purchased and used without further purification.

## 2.2. Synthesis of $\text{FeCu}_x$ composite material

The  $\text{FeCu}_x$  composite electrode materials were synthesized through a single series of autocatalytic Cu deposition and electroless Fe deposition, followed by washing with deionized water and vacuum drying at room temperature to acquire the precursor materials,  $\text{FeCu}_x$  ( $x=0, 0.1, 0.15, 0.2, 0.25, 0.3, 0.35$ ). The synthesis process of the  $\text{FeCu}_x/\text{FeS}/\text{C}$  microparticles is schematically presented in Fig. 1. The typical process to synthesize  $\text{FeCu}_{0.25}$  composite material was executed as follows:

16 g (0.3 mol) of Fe powder was dispersed into 400 ml deionized water to make 0.75M Fe dispersion. The dispersion was stirred on an overhead stirrer at 100 rpm for 10 minutes. 18.7 g of  $\text{CuSO}_4 \cdot 5\text{H}_2\text{O}$  (0.075 mol) was dissolved 200 ml deionized water to make 0.375 M  $\text{CuSO}_4$  solution by stirring at 100 rpm impeller speed for 2 mins on an overhead mixer. A 0.35 M  $\text{NaBH}_4$  solution was prepared by adding 12 g of  $\text{NaBH}_4$  into 900 ml deionized water and stirred at 100 rpm for 2 minutes on an overhead stirrer. Aqueous  $\text{CuSO}_4$  solution was added dropwise to the Fe dispersion under continuous stirring at 100 rpm. When the solution turned from blue to green, dropwise addition of the aqueous 0.55 M  $\text{NaBH}_4$  solution commenced under continuous stirring (at 100 rpm). The absence of gas bubbles together with a complete solution colour change from green to colourless indicated the successful reduction of residual  $\text{Fe}^{2+}$  ions; therefore, the composition of the composite was noted as  $\text{FeCu}_{0.25}$ . Correspondingly, the sample  $\text{FeCu}_x$  ( $x=0.2$ ) was also prepared by altering the mole ratio of Fe/Cu to 5 to suit the molecular denotation  $\text{FeCu}_{0.2}$ . After 10 minutes of continuous stirring (at 100 rpm) the mixture was allowed to cool down. The reaction products were separated by means of centrifugation, washed three times with deionized water, and finally dried in a vacuum oven at room temperature for 72 hours.

## 2.3. Synthesis of the $\text{FeCu}_x/\text{FeS}/\text{C}$ Composite Material

The optimum  $\text{FeCu}_{x=\text{optimum}}$  composite material was mixed (on an overhead mixer) with a varied amount of FeS (3, 6, 9, 12, 15%) to formulate the second set of electrode materials. All electrode formulations constituted 5% Graphite (Alfa Aesar, United States) and 5 % Coateylene (AXALTA, United States). Fig. 1 illustrates the synthesis process of the  $\text{FeCu}_x/\text{FeS}/\text{C}$  particles.

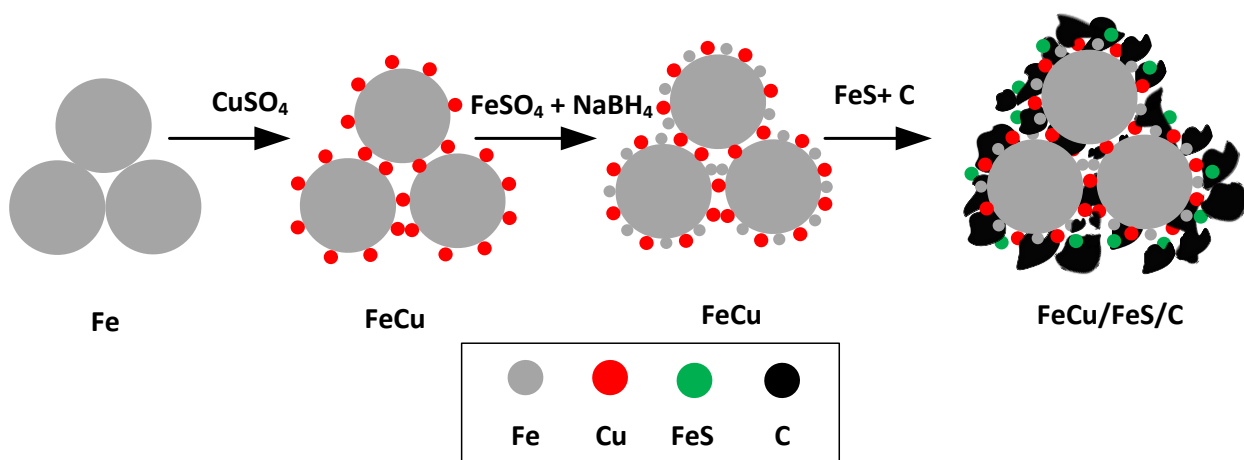


**Figure 1.** Schematic illustration of the synthesis process of the  $\text{FeCu}_x/\text{FeS}/\text{C}$  microparticles.

#### 2.4. Electrode Preparation

The composite materials were hot-pressed onto a nickel mesh using a custom-designed hydraulic press with integrated heated press plates (HyJack, Cape Town). The pressure of the hydraulic system was set at 3.9 MPa, which translates to a  $40 \text{ kg}_f \text{ cm}^{-2}$  on the sample. The pressing procedure was initiated after the pressure plates reached 100 °C. The compaction pressure on the sample was maintained for five minutes. The final electrode thickness and active material loading were  $0.75 \pm 0.10 \text{ mm}$  and  $0.16 \pm 0.05 \text{ g cm}^{-2}$  respectively. Two electrodes were produced for each electrode formulation:  $90 \text{ mm} \times 60 \text{ mm} \times 0.75 \text{ mm}$  for galvanostatic cycling measurements and  $10 \text{ mm} \times 10 \text{ mm} \times 0.75 \text{ mm}$  for cyclic voltammetry.

#### 2.5. Materials Characterization

The fresh electrode materials, as well as the charged and discharged electrode materials, were characterized by X-ray Diffraction (XRD) using a D8 Diffractometer (iThemba Labs, South Africa). Phase identification was done using DIFFRAC.EVA software and the plane reflections were indexed using the powder diffraction file (PDF). The nanostructure of the  $\text{FeCu}_x$  material was analysed by the Zeiss EM 912 CRYO EFTEM (EMU-University of Cape Town, South Africa). The morphology of the fresh Fe-matrix electrode samples, along with their respective charged/discharged electrodes, was assessed by TESCAN MIRA SEM with the Raman confocal system (EMU-University of Cape Town, South Africa).

#### 2.6. Electrochemical Characterisation

Cyclic voltammetry was conducted in a three-electrode set-up having the Fe-matrix as the working electrode, platinum (Pt) as the counter electrode and mercury/mercury oxide (4M KOH Hg/HgO) as the reference electrode. The electrodes, immersed in 6 M KOH/1M LiOH electrolyte, were activated for 50 cycles at a scan rate of  $200 \text{ mVs}^{-1}$  within a potential window of  $-1.4$  to  $-0.4 \text{ V}$  vs Hg/HgO.

Galvanostatic cycling measurements were conducted in a two-electrode set-up having the Fe-matrix as the working electrode, nickel oxy-hydroxide (NiOOH) as the counter electrode. To complete the setup the electrodes were immersed in a 6 M KOH/1M LiOH electrolyte.

In order to activate the electrodes, the cells were cycled for 30–40 cycles between 0.8 and 1.8 V at  $100 \text{ mA g}^{-1}$  current density. Thus, after being nominally “activated”, the electrodes were cycled between 0.8 and 1.75 V at  $100 \text{ mA g}^{-1}$  current density. All capacities reported in this work were after cell activation.

As for coulombic efficiency, when the cells were charged to 1.75 V at  $100 \text{ mAh g}^{-1}$ , the charge capacity was noted as  $Q_c$ . when the cells were discharged to 0.8 V at  $100 \text{ mAh g}^{-1}$ , the discharge capacity was noted as  $Q_d$ . The coulombic efficiency, denoted by  $\eta_c$ , was calculated using the  $[Q_d / Q_c \times 100\%]$  equation. In the rate capability tests, the discharge current was varied from 50 to  $600 \text{ mA g}^{-1}$  in increments.

To evaluate the polarization performance, the cells were charged to 1.75 V at 100 mAh g<sup>-1</sup>, and then discharged at a current density ranging from 200 to 2500 mAh/g for 5 s. All capacities are reported as per the mass of total Fe in the composite electrode.

Cyclic voltammetry was conducted by Metro Auto-Lab Set-up (PGSTAT128N 12 V / 800 mA). The electrochemical studies, such as the cycling stability and discharge rate capability, were performed, and the data acquired from NEWARE BTS-400 (5V 2A BTS System).

### 3. RESULTS AND DISCUSSION

#### 3.1 Materials Characterisation

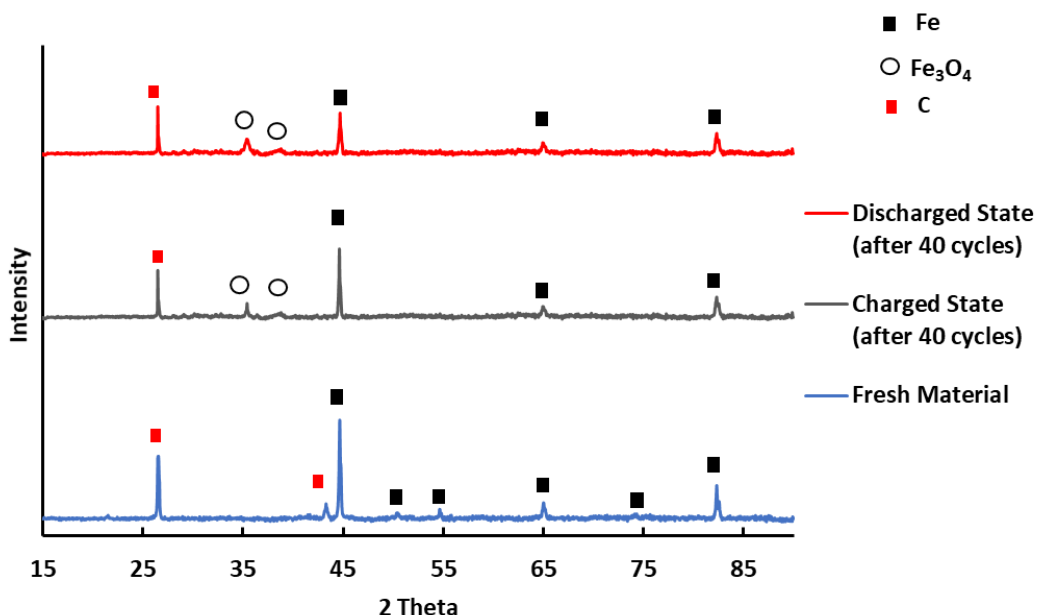
Fig. 2, 3 and 4 depict the XRD patterns of Fe/5%C, FeCu<sub>0.25</sub>/5%C and FeCu<sub>0.25</sub>/15%FeS/5%C composite electrodes respectively. The different crystal planes in the pattern are identified using the powder diffraction file directory (PDF numbers). The PDFs for Fe, Cu, FeS, C, Fe<sub>3</sub>O<sub>4</sub> and Cu<sub>2</sub>O are 00-006-0696, 00-004-0836, 00-037-0477, 00-026-1076, 00-019-0629 and 00-0050667 respectively.

In Fig. 2 peaks for Fe and C can be identified for the pure Fe sample. The (110) plane for Fe occurring at 2θ between 42.5 and 45.4 °, was the dominant facet for Fe in all the electrode formulations analysed. The crystallite size of fresh material particles is approximately 192 nm which decreased to 161 nm (after 40 cycles) due to particle surface passivation. Particle sizes were calculated using the Match! software which adopts the Scherrer equation. When the fresh material is deeply discharged, the XRD analysis of the pure Fe material shows that the peak intensity of Fe becomes weaker and the peaks of Fe<sub>3</sub>O<sub>4</sub> are observed. However, the variance between Fe peaks in fresh and discharged material is minimal, indicating a low utilisation of active material. In theory, the major discharge reaction product should be Fe(OH)<sub>2</sub>; however, it was not detected in the discharged state electrode material, suggesting that it was amorphous. The absence of Fe(OH)<sub>2</sub> was observed in all XRD results from discharged electrode materials. The decrease in Fe peak intensity between fresh Fe and charged electrode material might be ascribed to the limited reversibility of the electrochemical reaction.

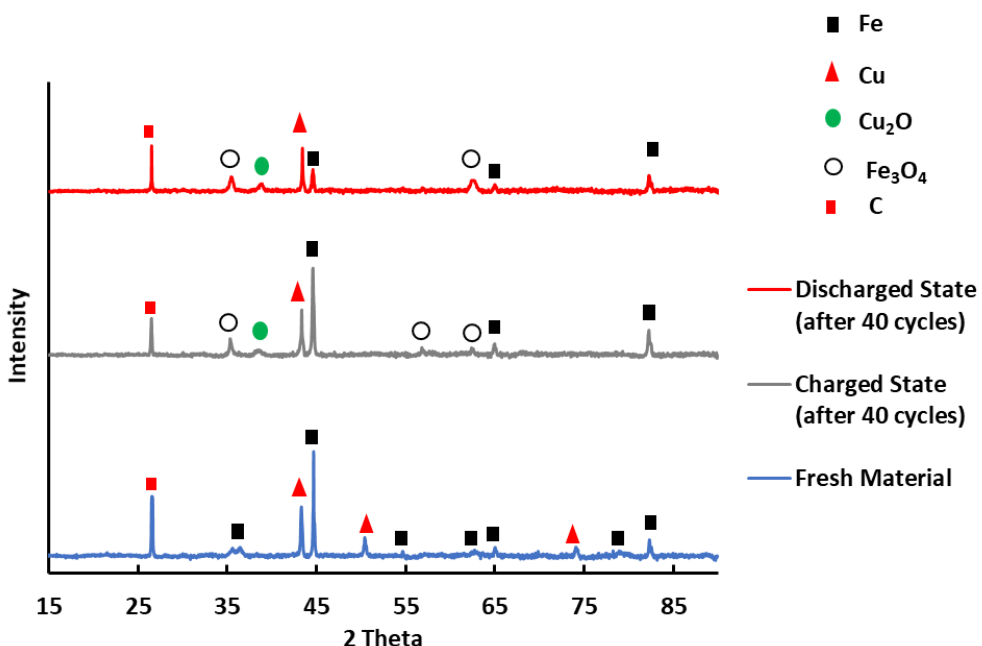
Fig. 3 shows that the fresh FeCu<sub>0.25</sub>/5%C composite material has strong peaks of Fe and weaker peaks of Cu which aligns with the ratio of Fe to Cu. When the fresh FeCu<sub>0.25</sub>/5%C composite material was deeply discharged, the XRD analysis indicated that the peaks of Fe become weaker and the peaks of Fe<sub>3</sub>O<sub>4</sub> are observed. The XRD analysis of the discharged FeCu<sub>0.25</sub>/5%C composite material also depicts that little Fe remains after deep discharge, indicating a high utilisation of active material compared to that of pure Fe electrode material. In addition, the peaks of Fe<sub>3</sub>O<sub>4</sub> are much stronger due to an increased amount of active material (Fe) participating in the electrochemical reaction. Furthermore, the peak of Cu<sub>2</sub>O was observed, indicating that some of the Cu was oxidized at a deep discharge state. The negligible decrease in Fe peak intensity between fresh FeCu<sub>0.25</sub>/5%C and charged FeCu<sub>0.25</sub>/5%C electrode material might be ascribed to the amplified reversibility of the electrochemical reaction induced by the ability of Cu to increase electro-conductivity of the electrode [10].

A relatively small reduction of the average FeCu<sub>0.25</sub> crystallite size was observed, i.e. from 141 nm at the start to 117 nm after 40-cycles. The lack of an anti-passivation agent in the electrode composite leads to surface passivation due to the inevitable formation of the discharge products (Fe<sub>2</sub>O<sub>3</sub> and

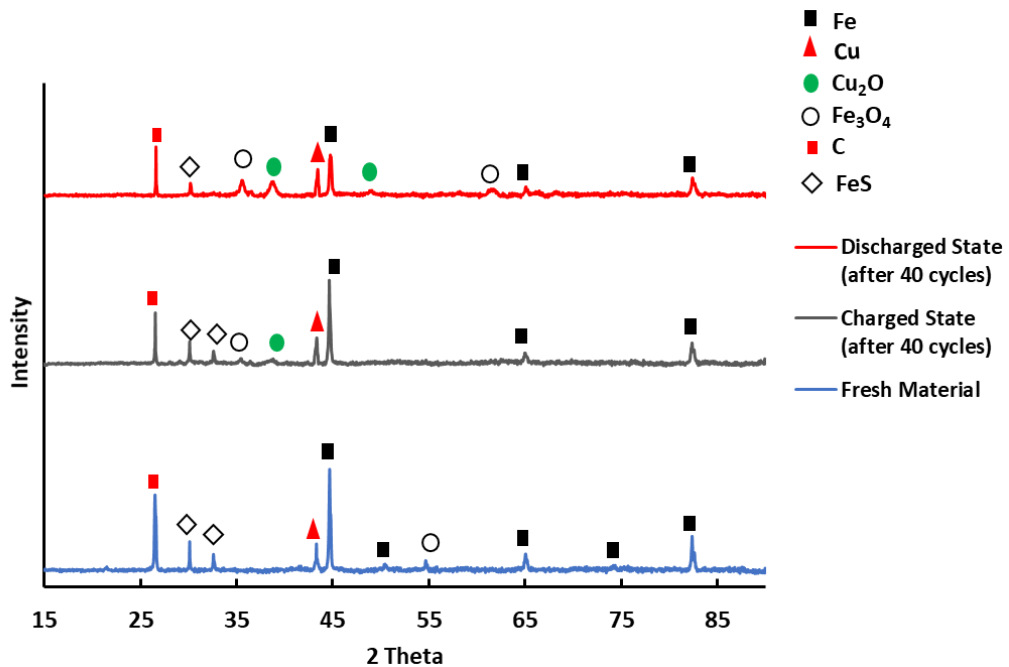
$\text{Fe}(\text{OH})_2$  which exhibit sparse electro-conductivity [4]. Fig. 4 shows the fresh  $\text{FeCu}_{0.25}/15\%\text{FeS}/5\%\text{C}$  composite material has strong peaks of Fe and weaker peaks of Cu and FeS which aligns with the formulations employed. The average crystallite size of the  $\text{FeCu}_{0.25}$  particles decreased from 139 to 121 nm after 40-cycles. This is due to the sulphur additive's ability to inhibit surface passivation [4,12,13]. The adsorption of  $\text{S}^{2-}$  (from the FeS additive) onto the Fe- $\text{Fe}(\text{OH})_2$  particle structure fosters a distortion that leads to an increase in defect concentration of the film and consequently, an increase in its ionic conductivity. This mechanism retards the passivation process, subsequently leading to the formation of a thicker film.



**Figure 2.** XRD patterns for F/5%C electrode.

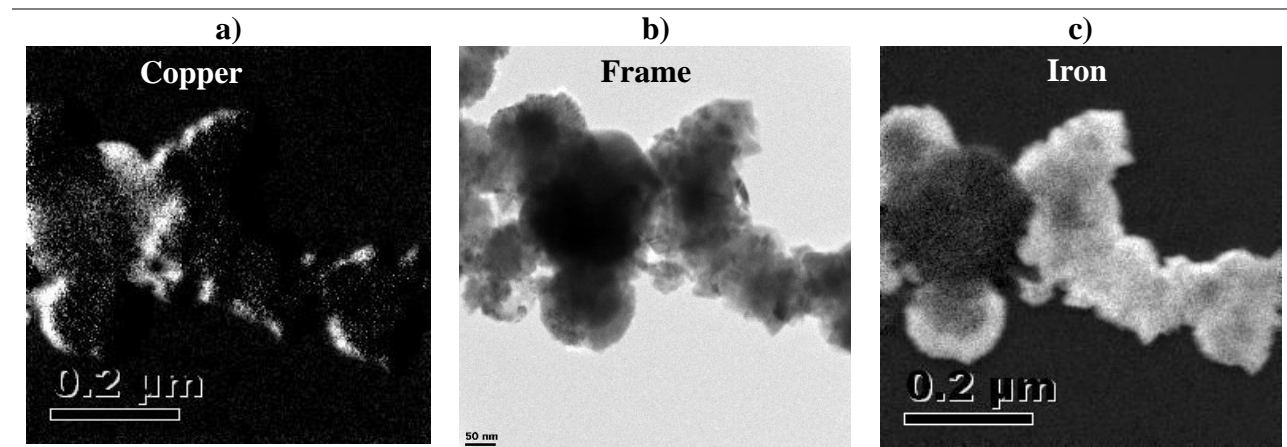


**Figure 3.** XRD patterns for  $\text{FeCu}_{0.25}/5\%\text{C}$  electrode.



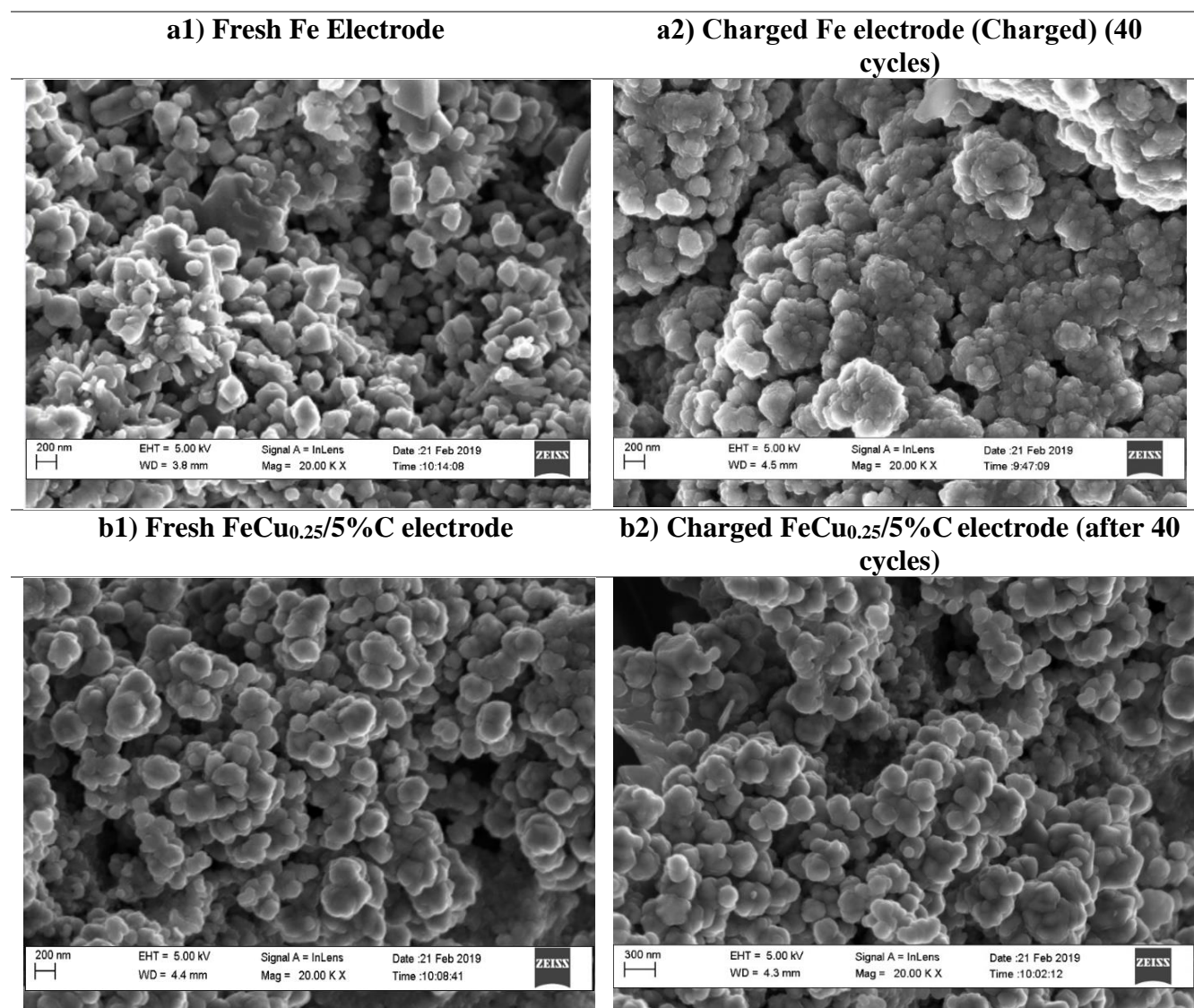
**Figure 4.** XRD patterns for  $\text{FeCu}_{0.25}/15\%\text{FeS}/5\%\text{C}$  electrode.

Fig. 5 shows the energy-filtered transmission electron microscopy (EFTEM) imaging of the  $\text{FeCu}_{0.25}$  composite material to confirm the Fe-core Cu-shell particle arrangement. It is evident from Figs. 4 a-c that the particles are in a Fe core Cu coat structure with particle sizes in a typical range of 150 to 250 nm. In Figs. 5a and 5c, the light portion of the image represents the Cu and Fe distribution respectively. Because a part of Fe was oxide and dissolved  $\text{Fe}^{2+}$  was reduced back to elemental Fe after initial Cu precipitation, the coating layer contained Cu and some Fe as depicted by EFTEM imaging (Fig. 5).



**Figure 5.**  $\text{FeCu}_{0.25}/5\%\text{C}$  material EFTEM imaging analysis.

Figs. 6 a1 and a2 show the scanning electrode microscopy (SEM) images for the Fe/5%C in a fresh and charged state respectively, while Figs. 6 b1 and 6 b2 show the SEM images for the FeCu<sub>0.25</sub>/5%C electrode in a fresh and charged state. The FeCu<sub>0.25</sub>/5% composite particles were prepared by a two-step method that included Cu electroless deposition and reduction. The original Fe particles (visible in Fig 6.a1) appear cubical with particle size ranging from 150-250nm. When Cu was autocatalytically deposited onto Fe particles and subsequently subjected to electroless plating with Fe using the NaBH<sub>4</sub>, particles appear more spherical and larger with a particle size distribution between 200 and 300nm ((visible in Fig6.b1). The shape of nanoparticles is primarily dependant on surface energy minimization; therefore, rather intuitively, spherical or roughly spherical polyhedral shapes with the lowest surface-to-volume ratio are the most likely to form in a process which is characterised by spontaneous chemical kinetics [18]. The SEM images in Figure 6a2 and 6b2 confirm that the FeCu<sub>0.25</sub>/5%C based composites inhibit particle agglomeration upon cycling, compared to pure Fe material, which indicates visible particle agglomeration after 40 cycles as depicted in Fig. 6a2.



**Figure 6.** SEM images for a) Fe/5%C electrode and b) FeCu<sub>0.25</sub>/5%C electrode.

### 3.2 Electrochemical Characterisation

Fig. 7 shows the cyclic voltammograms of the Fe/5%C, FeCu<sub>0.25</sub>/5%C composite and FeCu<sub>0.25</sub>/15%FeS/5%C composite electrodes. The electrodes were activated for 50 cycles at a scan rate of 200 mVs<sup>-1</sup> vs. the Hg/HgO in 6 M KOH/1M LiOH electrolyte. The activation step was executed to remove any surface impurities and stabilize the electrode's electrochemical response. The graph shows the cyclic voltammograms obtained after the 30th cycle at a scan rate of 2.5 mVs<sup>-1</sup> vs. the Hg/HgO in 6 M KOH/1 M LiOH electrolyte.

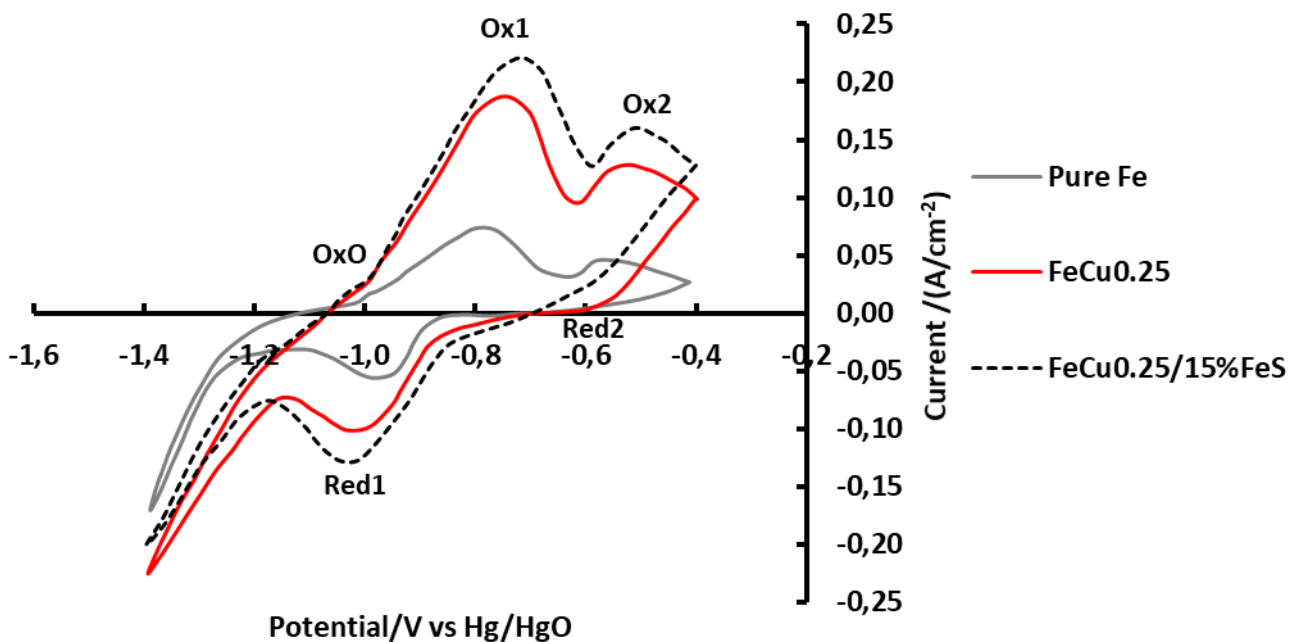


**Figure 7.** Cycling voltammetry of pure Fe/5%C electrode, FeCu<sub>0.25</sub>/5%C electrode and FeCu<sub>0.25</sub>/15%FeS/5%C electrode in 6M KOH /1M LiOH at 2mV/s.

All three cyclic voltammograms depict two major oxidation peaks (Ox1 and Ox2) for Fe as well as an additional small pre-peak (Ox0) due to hydrogen oxidation and hydroxyl ion adsorption i.e.  $H_2 \rightarrow 2H_2O$  [4]. The peak Ox1 corresponds to the  $Fe \rightarrow Fe(OH)_2$  while Ox2 corresponds to the  $Fe(OH)_2 \rightarrow Fe_3O_4$  reaction [7,10,19]. The phenomenon of the removal of adsorbed hydrogen from the electrode during the anodic sweeping has also been observed by the electrochemical quartz crystal microbalance method, confirming the initial Fe/Fe(II) reaction step [20]. The Ox1 reaction is more favoured under the test conditions and appears twice as large as the Ox2 peak which indicates that there is a significantly higher charge associated with it. However other literature reports have shown a larger or equal-sized Ox2 peak compared to the Ox1 peak [21–24]. A possible explanation for the smaller Ox2 peak could be due to partial oxidation which is limited by repulsion from the neighbouring Fe (II) sites. The ratio of the oxidation peaks may also be dependent on the type of Fe material analysed and the type of additives incorporated. The Ox1 peaks show maximum peak heights at  $-0.78$  V,  $-0.75$  V and  $-0.72$  V for the Fe/5%C, FeCu<sub>0.25</sub>/5%C and FeCu<sub>0.25</sub>/15%FeS/5%C electrodes respectively. The Ox2 peaks show

maximum peak heights at  $-0.56$  V,  $-0.52$  V and  $-0.51$  V for the Fe/5%C, FeCu<sub>0.25</sub>/5%C and FeCu<sub>0.25</sub>/15%FeS/5%C electrodes respectively. The addition of Cu shifts the oxidation potential to slightly less negative potential. This shift implies a lowering in over-potential. It was reported that the oxidation of Cu to Cu<sub>2</sub>O takes place at  $-0.4641$  V vs Hg/HgO [15,25]. In the case of the FeCu<sub>0.25</sub>/5%C electrode, the oxidation of Cu may also exist in parallel with the Fe (II)/Fe (III), though its peak was not distinct due to its relatively small amount in the electrode composite. The Red1 peaks, corresponding to the reduction of Fe (II) to Fe(0), show maximum peak heights at  $-0.98$  V,  $-1$  V and  $-1$  V for the pure Fe/5%C, FeCu<sub>0.25</sub>/5%C and FeCu<sub>0.25</sub>/15%FeS/5%C electrodes respectively. Clear peaks on the reduction of Fe<sub>3</sub>O<sub>4</sub> to Fe(OH)<sub>2</sub> were not observed in any of the voltammograms, as this reaction would have preceded the Fe(OH)<sub>2</sub>/Fe reduction peaks [26,27]. However, it cannot be ruled out that the reduction peak is an overlap of both the Fe(III)/Fe(II) and Fe(II)/Fe(0) reduction reactions as these two reduction reactions both occur within a very small potential window [21,22,28]. Following this peak, however, the hydrogen evolution reaction becomes predominant at a potential which is more negative than  $-1.16$  V. The Fe/5%C electrode shows the smallest redox peaks compared to the FeCu<sub>0.25</sub>/5%C composite and FeCu<sub>0.25</sub>/15%FeS/5%C composite electrodes which indicates a lower ability of the electrode to store charge. The specific capacitance ( $C_s$ ) was calculated using the following equation:

$$C_s = \frac{\int IdV}{mv\Delta V} \quad [3]$$

Where  $C_s$  is specific capacitance (Fg<sup>-1</sup>),  $\int IdV$  is the area under the anodic curve, m is the mass of the active electrode material (g), v is the scan rate (Vs<sup>-1</sup>) and  $\Delta V$  is the potential window (V). The calculated specific capacitances for the pure Fe, FeCu<sub>0.25</sub> composite and FeCu<sub>0.25</sub>/15%FeS composite electrodes are 84.7 Fg<sup>-1</sup>, 233.3 Fg<sup>-1</sup> and 286.7 Fg<sup>-1</sup> respectively. Furthermore higher cathodic current densities are observed with the addition of Cu (from 74 to 188 mA cm<sup>-2</sup>) which is beneficial for battery operations and utilization at high discharge rates [19]. The increased cathodic current density could be attributed to the better electronic conductivity displayed by the metallic Cu present in the composite material [10]. The addition of FeS effectuated a further increase in cathodic current density to 220 mA cm<sup>-2</sup> which could be due to the beneficial role of FeS in improving the ionic conductivity of the passivation layer [22]. The sulphide which is released from the sulphide additive attaches to the Fe electrode particles to modify its morphology [12,29]. This results in the restraining of the formation of the passive Fe(OH)<sub>2</sub> layer, enhancing the bulk conductivity of the Fe electrode and blocking the electrochemical process of hydrogen evolution [23]. It should be noted that the addition of Cu also decreases the anodic current density of the hydrogen evolution reaction which is not beneficial for the charging process. The addition of the FeS to the FeCu<sub>0.25</sub>/5%C composite is shown to lower the hydrogen evolution reaction anodic current density as expected.

Fig. 8 displays the discharge curves of Fe/5%C, FeCu<sub>0.25</sub>/5%C and FeCu<sub>0.25</sub>/15%FeS/5%C composite electrode materials while Fig. 9 displays the polarization curves of Fe/5%C, FeCu<sub>0.25</sub>/5%C and FeCu<sub>0.25</sub>/15%FeS/5%C composite electrode materials.

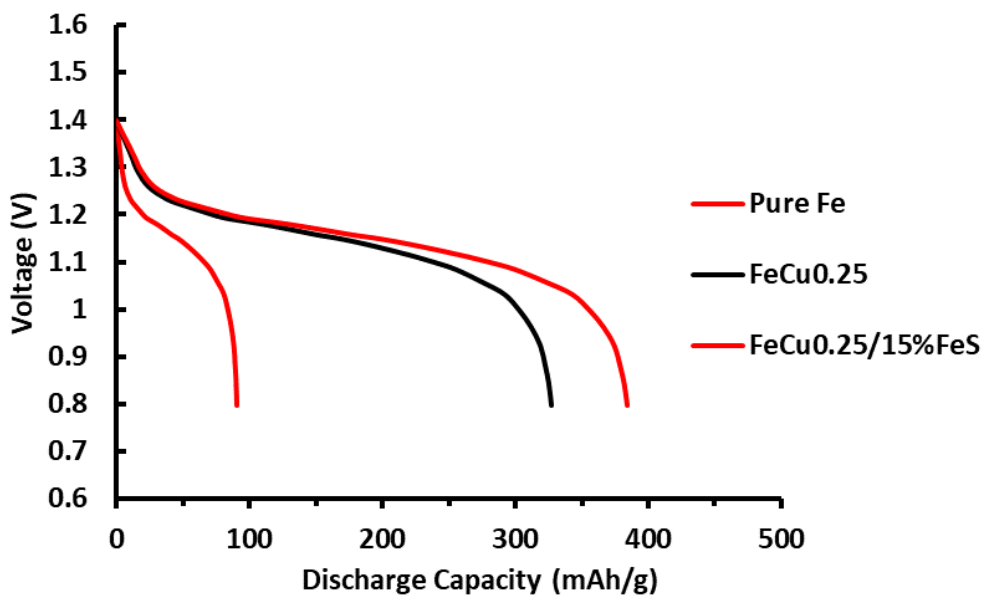


**Figure 8.** Discharge curves of Fe/5%C, FeCu<sub>0.25</sub>/5%C and FeCu<sub>0.25</sub>/15%FeS/5%C composite electrode materials: The cells were charged at 100mA/g to 1.75 V, and then discharged at 100 mA/g C to 0.8 V.

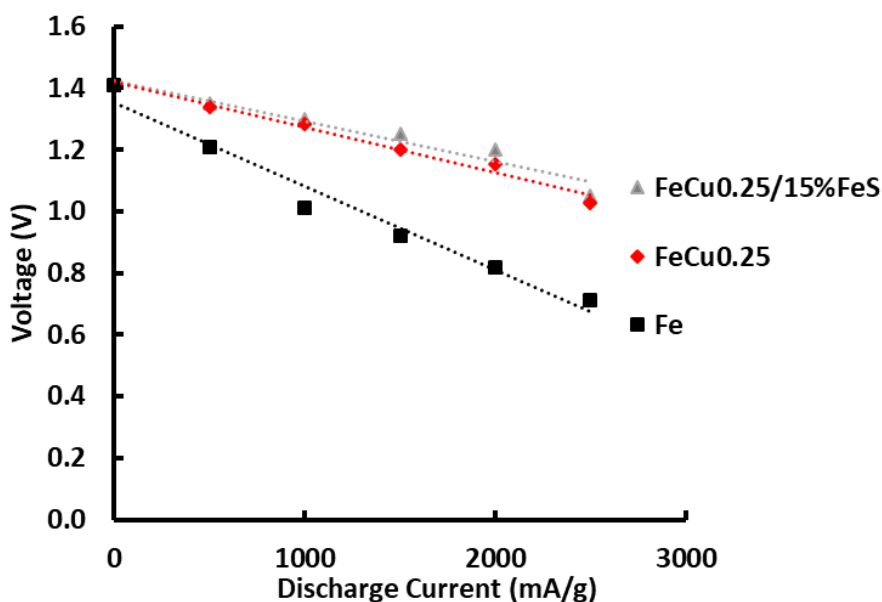


**Figure 9.** Polarization curves of Fe/5%C, FeCu<sub>0.25</sub>/5%C and FeCu<sub>0.25</sub>/15%FeS/5%C electrodes: the cells were charged at 1000 mA/g for 90 min, and then discharged at a rate ranging from 200 mA/g C to 2500 mA/g for 5 s.

It is noteworthy that the activation process is a fundamental step in secondary alkaline battery technology. Generally, Fe electrodes always suffer from slow activation progress in the first cycles compared to other analogous electrodes (Ni, Zn, Na, Air, Al etc)[10]. The discharge curve of pure Fe had only one plateau which suggested the conversion of Fe to Fe(OH)<sub>2</sub>. The capacity was about 90 mAh g<sup>-1</sup>, significantly lower than the theoretical value for Fe of 962 mAhg<sup>-1</sup>[8]. This large deviation was influenced chiefly by the parasitic hydrogen evolution side reaction and significant particle agglomeration [12,16,26]. The discharge curves of Fe/5%C, FeCu<sub>0.25</sub>/5%C and FeCu<sub>0.25</sub>/15% FeS/5%C

had exhibited only one plateau which suggested the conversion of Fe to  $\text{Fe(OH)}_2$  [2,29]. The capacity of the  $\text{FeCu}_{0.25}$  electrode material capacity was about  $340 \text{ mAh g}^{-1}$ , significantly higher than the capacity of pure Fe electrode material. The higher capacity was due to the presence of Cu particles constructing an electron transfer network for the oxidation and reduction of  $\text{Fe}/\text{Fe(II)}$  reaction to progress. Because  $\text{NaBH}_4$  was used as the reducing agent, the generation and incorporation of hydrogen into Fe could, therefore, be expected [2]. During the discharge of Fe, hydrogen could react with  $\text{OH}^-$  to produce water. This reaction may contribute to the extra electrical capacity of the electrode [3]. The capacity  $\text{FeCu}_{0.25}/15\%\text{FeS}$  electrode exhibited similar discharge behaviour to  $\text{FeCu}_{0.25}/5\%\text{C}$  but delivered a slightly higher specific capacity of  $380 \text{ mAh g}^{-1}$ . The slightly higher capacity was due to the presence of FeS that aids in circumventing the hydrogen evolution reaction and enhancing the electrode's ionic conductivity; consequently the electrode accepts and transports more charge [4,29]. Fig. 9 showed the polarization curves of  $\text{Fe}/5\%\text{C}$ ,  $\text{FeCu}_{0.25}/5\%\text{C}$  and  $\text{FeCu}_{0.25}/15\%\text{FeS}/5\%\text{C}$  composite electrode materials. As the current densities are increased, the polarization becomes intensified. However, as represented in Fig. 14., the polarization of  $\text{FeCu}_{0.25}/5\%\text{C}$  composite electrode (which co-aligns with  $\text{FeCu}_{0.25}/15\%\text{FeS}/5\%\text{C}$ ), is less intense (less ohmic potential drops), compared to the pure Fe electrode. This is attributed to the ability of Cu particles to construct an electro-conductive network for the redox reaction to progress.

In Fig. 10, the capacities of the electrode materials constituting different amounts of Cu were shown in up to 40 cycles. The battery was operated between 1.75 V and 0.8 V at a current density of  $100\text{mA g}^{-1}$ .

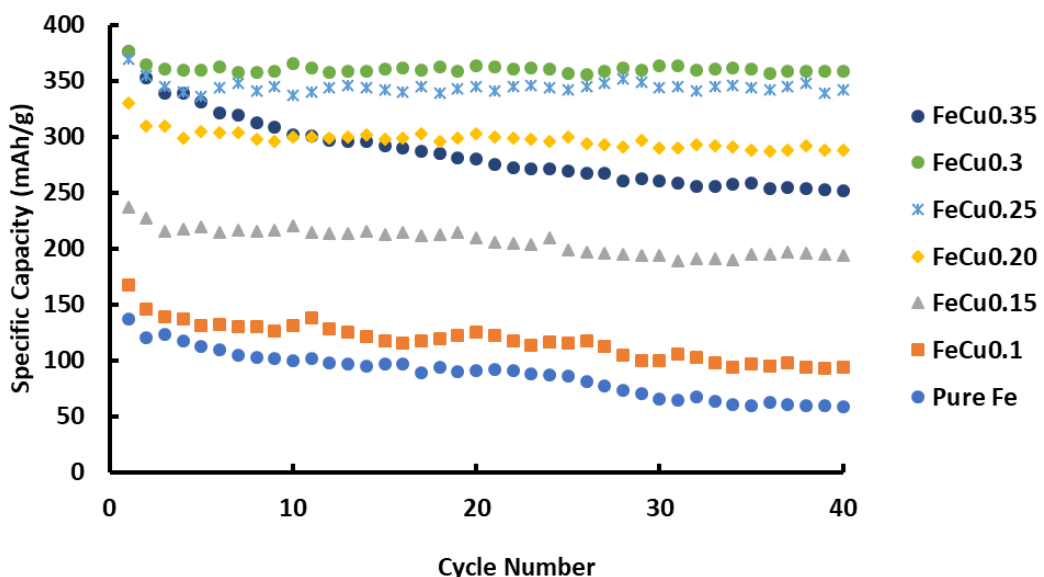


**Figure 10:** Cycling stability curves of pure  $\text{Fe}/5\%\text{C}$  and various  $\text{FeCu}_x/5\%\text{C}$  composite electrodes: the cells were charged at  $100\text{mA/g}$  to 1.75 V, and then discharged at  $100 \text{ mA/g}$  C to 0.8 V.

The discharge capacities of the composite electrodes increase gradually with Cu content. The capacity of the pure Fe electrode decreased quickly to around  $100 \text{ mAhg}^{-1}$  at about 10 charge-discharge cycles. From ten cycles onwards, the specific capacity of  $\text{Fe}/5\%\text{C}$  gradually decreases with the

cycle number. This is due to reduced particle surface area due to massive particle agglomeration as noted in the SEM image depicted in Fig. 6a2. The highest capacity of around  $360 \text{ mAh g}^{-1}$  was attained when the  $\text{FeCu}_{0.25}$  composite electrode material was employed. The electrode exhibited superlative cycling stability as it retained more than 95% of the initial capacity. This is attributed to the ability of Cu to lower the particle surface energy through its highly conductive network embedded in the electrode [10]. When the material was  $\text{FeCu}_{0.1}$ , the effect of Cu content was only minimal and directly comparable to the pure Fe electrode. At this stage, the copper may not have been sufficient to form an electron-conducting network to aid with the oxidation/reduction electrode reactions and/or to prevent particle agglomeration. On the other hand, when the Cu addition is over  $\text{FeCu}_{0.3}$ , the Cu might cover the entire Fe particle active surface and therefore the electrode exhibited a lower specific capacity [2]. In an attempt to limit utilisation of high amounts of costly Cu, the optimum Cu composition was  $\text{FeCu}_x$  ( $x=0.25$ ), since there was no significant difference between  $\text{FeCu}_x$  ( $x=0.25$ ) and  $\text{FeCu}_x$  ( $x=0.3$ ) in terms of specific capacity and cycling stability. The nominal capacity of  $350 \text{ mAh g}^{-1}$  (Fe) is a promising number for future applications in renewable energy storage systems (RESS).

In Fig. 11, the specific capacities of the  $\text{FeCu}_{0.25}/5\%$ C electrode materials containing different amounts of FeS were depicted (capacity values up to 40 cycles).

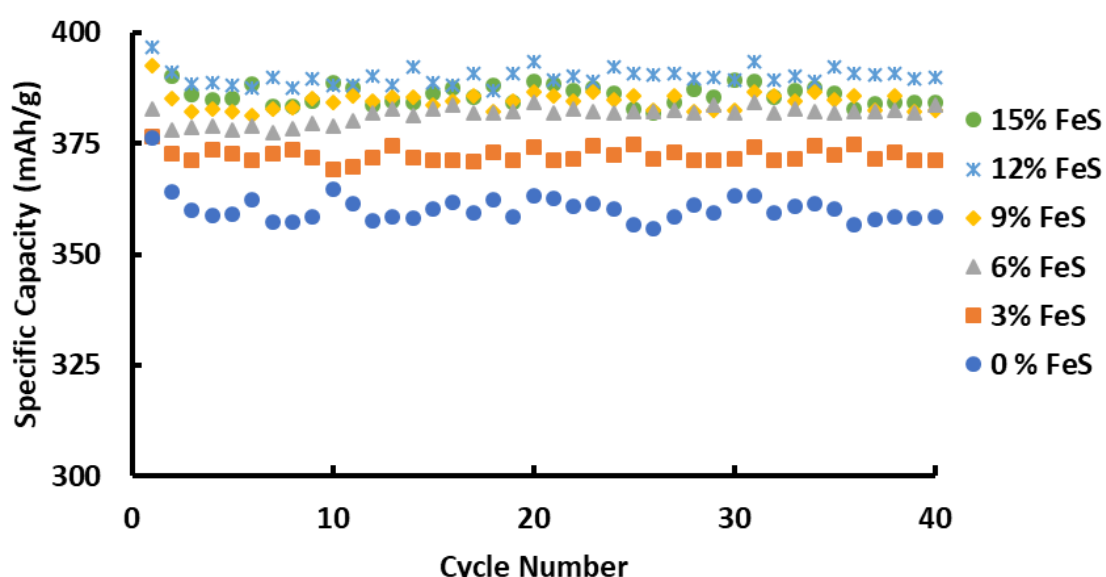


**Figure 11.** Specific capacity versus % FeS Content in  $\text{FeCu}_{0.25}/5\%$ C electrode material (capacity values up to 40 cycles): The cells were charged at  $100 \text{ mA/g}$  to  $1.75 \text{ V}$ , and then discharged at  $100 \text{ mA/g}$  C to  $0.8 \text{ V}$ .

In Fig. 12, the capacities of the  $\text{FeCu}_{0.25}/5\%$ C electrode materials containing different amounts of FeS were depicted (specific capacity at the 10<sup>th</sup> cycle).

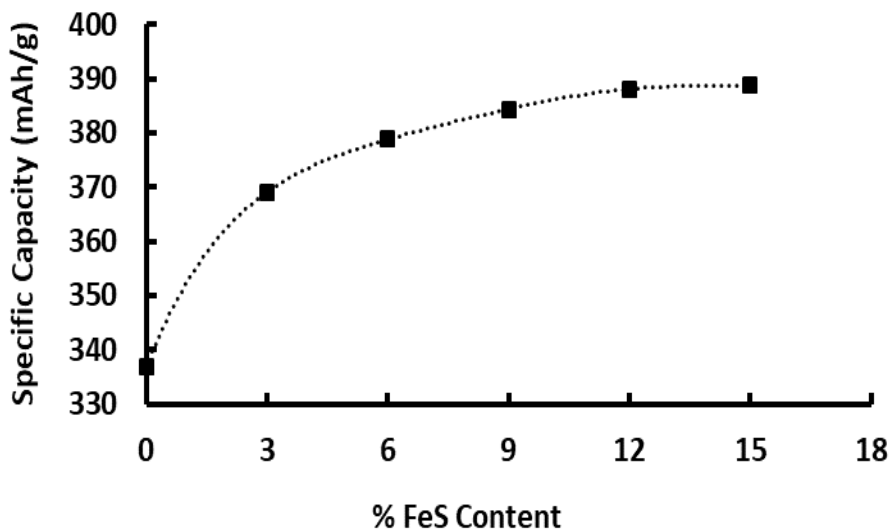


**Figure 12.** Specific capacity versus % FeS Content in  $\text{FeCu}_{0.25}/5\%\text{C}$  electrode material: The cells were charged at 100mA/g to 1.75 V, and then discharged at 100 mA/g C to 0.8 V.

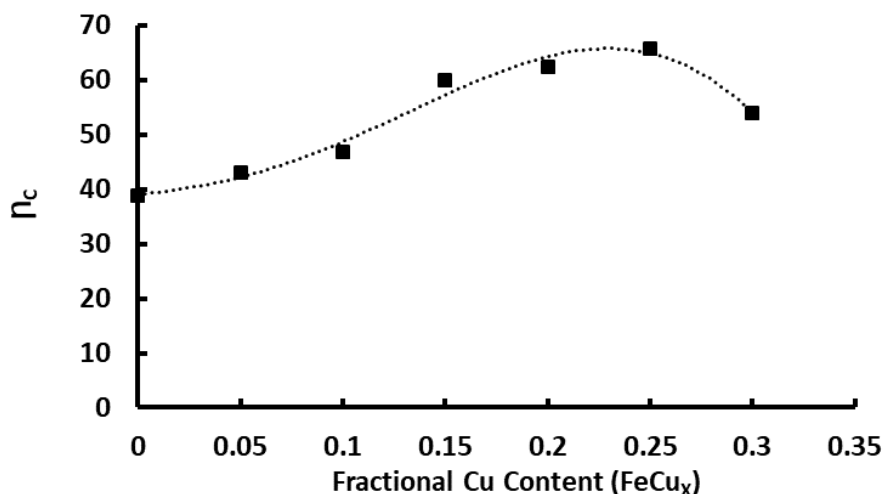


**Figure 13.** Coulombic efficiency of Fe-based electrodes containing various amounts of Cu: The cells were charged at 100mA/g to 1.75 V, and then discharged at 100 mA/g C to 0.8 V.

The highest capacity of around  $390 \text{ mAh g}^{-1}$  was attained when 15% FeS was incorporated into the  $\text{FeCu}_{0.25}$  electrode composite material. As % FeS content increases, the specific capacity increases up until capacity stabilization at %FeS Content>12. The linear correlation is attributed to the ability of FeS to partake in the electrochemical reaction and its ability to distort the  $\text{Fe(OH)}_2$  structure which leads to an increase in defect concentration of the film, consequently increasing its ionic conductivity [4,12,29]. The capacity stabilises at %FeS Content>12. At higher FeS concentrations (>20%), the

capacity drastically drops, nevertheless, this effect is not completely understood [3]. Fig. 12 displays the coulombic efficiency of the charging process for electrodes containing various amounts of FeS.

Fig. 13 displays the coulombic efficiency of the electrodes containing various amounts of copper. As the fractional copper content increases, the coulombic efficiency increases. This is attributed to the ability of Cu electro-conductive network to amplify reversibility of the  $\text{Fe}(3+)/\text{Fe}(2+)/\text{Fe}(0)$  reaction [19,30]. The presence of Cu nanoparticles increases the overvoltage of the hydrogen evolution, consequently effectuating an upswing in the charge efficiency [6].

Fig. 14 displays the coulombic efficiency of the  $\text{FeCu}_{0.25}/5\%\text{C}$  electrodes containing different amounts of FeS additive.

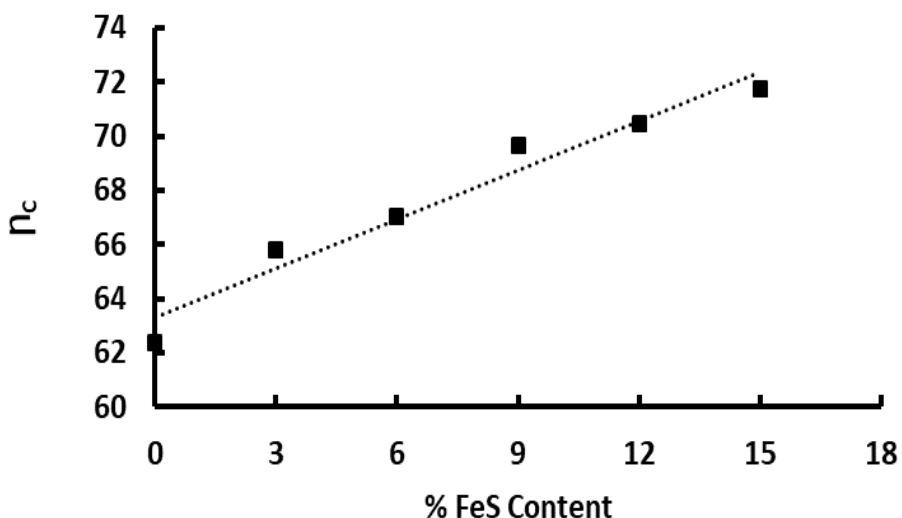


**Figure 14.** Coulombic efficiency versus % FeS content in  $\text{FeCu}_{0.25}/5\%\text{C}$  electrode material: The cells were charged at 100mA/g to 1.75 V, and then discharged at 100 mA/g C to 0.8 V.

As % FeS content increases, the coulombic efficiency increases; this is attributed to the ability of FeS to increase the overvoltage of the hydrogen evolution reaction. The coulombic efficiency of 71 % was attained when the electrode formulation of 15% FeS in  $\text{FeCu}_{0.25}/5\%\text{C}$  electrode material was employed; however, it has been reported that higher FeS (>15%) tends to shorten the life of the battery; thus in this work, the cut off value for %FeS composition was 15% [5,12,26,29]. The high charge and coulombic efficiency induced by FeS through amplified electrochemical reaction reversibility and curbing hydrogen evolution reaction are due to the adsorption of the highly polarizing  $\text{S}^{2-}$  ion on the  $\text{Fe}-\text{Fe}(\text{OH})_2$  particles. [29]. Hydrogen molecular recombination reaction equation [1] is inhibited by  $\text{S}^{2-}$  ion chemisorption [31]. Another influential factor is the change of electrode surface species prompting the overpotential of the hydrogen evolution reaction [13,29].

Fig. 15 depicts the discharge rate capability of  $\text{FeCu}_{0.25}/5\%\text{C}$  and  $\text{Fe}/5\%\text{C}$  electrode.

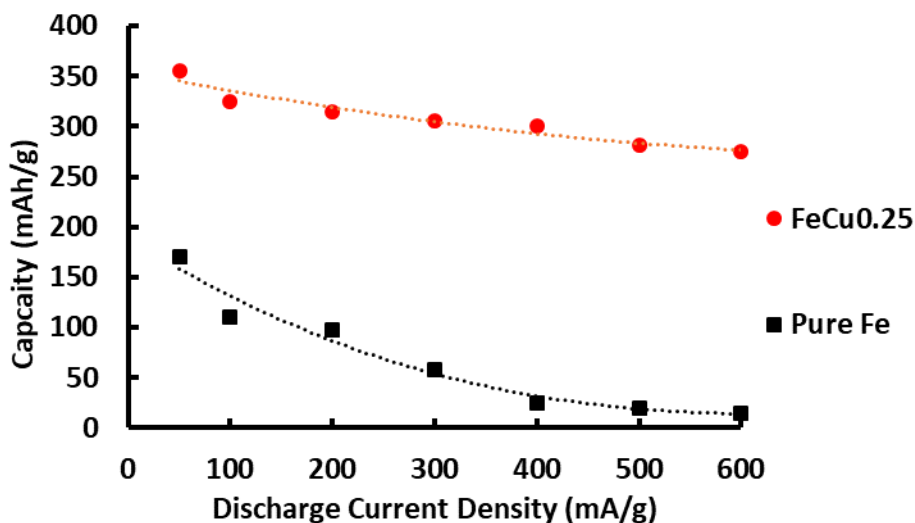


**Figure 15.** Discharge capability at different current densities for Fe/5%C and FeCu<sub>0.25</sub>/5%C electrode materials: the cells were charged at 100mA/g to 1.75 V, and then discharged at rates from 50 to 600 mA/g to 0.8 V.

The Fe/5%C electrode performs poorly at higher discharge rates. This is indicated by the drastic drop in the specific capacity as the current density increases. The FeCu<sub>0.25</sub>/5%C electrode material exhibits the best rate in performance, even at an impressively high rate of 600 mA g<sup>-1</sup> and a specific discharge capacity of about 300 mAh g<sup>-1</sup> is achieved with 85 % of the nominal capacity retained. This indicates that the FeCu<sub>x</sub> composite electrode materials show significant potential as a high-rate electrode material for Fe-based rechargeable batteries. This inimitable high rate discharge capability is attributed to the ability of Cu to improve the electron transfer between Fe particles by constructing a stable electron transfer network [2,19]. Generally, the discharge rate capability of the pure Fe electrodes was limited to 600 mA g<sup>-1</sup> due to the inevitable rampant bulk formation of a Fe(OH)<sub>2</sub> passive layer [2].

#### 4. CONCLUSION

A series of FeCu<sub>x</sub> composite electrode materials were synthesized by autocatalytic Cu deposition followed by electroless Fe deposition, of which some of the materials were doped with various amounts of FeS. The inclusion of both Cu and FeS revealed a drastic increase in the specific charge/discharge capacity, stability and coulombic efficiency. The Cu nanoparticles in the FeCu<sub>0.25</sub>/5%C composite construct formed a stable network to transfer electrons during the reduction/oxidation of the Fe electrode. The incorporation of Cu, therefore, prevents the fast drop in electrical capacity induced by the formation of a non-conductive Fe(OH)<sub>2</sub> layer. The inclusion of FeS further increases the efficiency of the electrode by curbing the parasitic hydrogen evolution and enhancing the ionic conductivity of the passivation layer. Ultimately, the FeCu<sub>0.25</sub>/15%FeS/5%C composite electrode material delivers a stable capacity of about 385 mAh g<sup>-1</sup> with ~ 70% coulombic efficiency at a current density of 100 mA g<sup>-1</sup>. The electrode

material can still deliver about 278 mAh g<sup>-1</sup> at a high current density of 600 mA g<sup>-1</sup>. This outcome thus opens the possibility of future applications for the development of advanced Fe-based alkaline batteries with performance characteristics required for integration with renewable energy resources.

## ACKNOWLEDGEMENTS

Funding provided by Eskom South Africa and the Department of Science and Technology (DST) South Africa, in order to execute this research project, is gratefully acknowledged.

## References

1. D. Gielen, F. Boshell, D. Saygin, M.D. Bazilian, N. Wagner, R. Gorini, *Energy Strateg. Rev.*, 24 (2019) 38–50.
2. C.-Y. Kao, Y.-R. Tsai, K.-S. Chou, *J. Power Sources*, 196 (2011) 5746–5750.
3. J.O.G. Posada, A.J.R. Rennie, S.P. Villar, V.L. Martins, J. Marinaccio, A. Barnes, C.F. Glover, D.A. Worsley, P.J. Hall, *Renew. Sustain. Energy Rev.*, 68 (2017) 1174–1182.
4. J.O.G. Posada, P.J. Hall, *J. Appl. Electrochem.*, 46 (2016) 451–458.
5. A.H. Abdalla, C.I. Oseghale, J.O.G. Posada, P.J. Hall, 10 (2016) 1529–1534.
6. J.O. Gil Posada, A.H. Abdalla, C.I. Oseghale, P.J. Hall, *Int. J. Hydrogen Energy*, 41 (2016) 16330–16337.
7. A.R. Paulraj, Y. Kiros, M. Chamoun, H. Svengren, D. Noréus, M. Göthelid, B. Skärman, H. Vidarsson, M.B. Johansson, *Batteries*, 5 (2018).
8. H. Zhao, Q. Wu, S. Hu, H. Xu, C.N. Rasmussen, *Appl. Energy*, 137 (2015) 545–553.
9. T. Reddy, Linden's Handbook of Batteries, (2010).
10. L. Huang, J. Yang, P. Liu, D. Zhu, Y. Chen, *Int. J. Electrochem. Sci.*, 13 (2018) 7045–7056.
11. A.K. Manohar, S. Malkhandi, B. Yang, C. Yang, G.K. Surya Prakash, S.R. Narayanan, *J. Electrochem. Soc.*, 159 (2012) A1209–A1214.
12. C.A. Caldas, M.C. Lopes, I.A. Carlos, *J. Power Sources*, 74 (1998) 108–112.
13. B.T. Hang, T. Watanabe, M. Egashira, I. Watanabe, S. Okada, J. Ichi Yamaki, T. Reddy, A.K. Manohar, S. Malkhandi, B. Yang, C. Yang, G.K. Surya Prakash, S. Malkhandi, G.K.S. Prakash, S.R. Narayanan, J.O.G. Posada, P.J. Hall, A.H. Abdalla, C.I. Oseghale, P.J. Hall, A.J.R. Rennie, S.P. Villar, V.L. Martins, J. Marinaccio, A. Barnes, C.F. Glover, D.A. Worsley, P.J. Hall, D. Sarkar, A.K. Shukla, D.D. Sarma, Q. Wang, Y. Wang, C.A. Caldas, M.C. Lopes, I.A. Carlos, A.R. Paulraj, Y. Kiros, M. Chamoun, H. Svengren, D. Noréus, M. Göthelid, B. Skärman, H. Vidarsson, M.B. Johansson, T.M.D. Dang, T.T.T. Le, E. Fribourg-Blanc, M.C. Dang, L. Huang, J. Yang, P. Liu, D. Zhu, Y. Chen, W. Jiang, F. Liang, J. Wang, L. Su, Y. Wu, L. Wang, C.-Y. Kao, Y.-R. Tsai, K.-S. Chou, B. Yang, A.K. Manohar, G.K.S. Prakash, S.R. Narayanan, S. Al Jaber, R. Burrett, M. Eckhart, D. Hales, R. Hosier, A.S. Rajan, M.K. Ravikumar, K.R. Priolkar, S. Sampath, A.K. Shukla, *J. Power Sources*, 135 (2016) 5746–5750.
14. A.K. Manohar, C. Yang, S.R. Narayanan, *ECS Meet. Abstr.* (2016).
15. A.K. Manohar, C. Yang, S. Malkhandi, G.K.S. Prakash, S.R. Narayanan, *J. Electrochem. Soc.*, 160 (2013).
16. A.S. Rajan, M.K. Ravikumar, K.R. Priolkar, S. Sampath, A.K. Shukla, O. Access, 1 (2014) 2–9.
17. K. Vijayamohan, T.S. Balasubramanian, A.K. Shukla, *J. Power Sources*, 34 (1991) 269–285.
18. J. Zhao, E. Baibuz, J. Vernieres, P. Grammatikopoulos, V. Jansson, M. Nagel, S. Steinhauer, M. Sowwan, A. Kuronen, K. Nordlund, F. Djurabekova, *ACS Nano*, 10 (2016) 4684–4694.
19. A.R. Paulraj, Y. Kiros, B. Skärman, H. Vidarsson, *J. Electrochem. Soc.*, 164 (2017) A1665–A1672.
20. S. Joiret, M. Keddam, X.R. Nóvoa, M.C. Pérez, C. Rangel, H. Takenouti, *Cem. Concr.*

- Compos.*, 24 (2002) 7–15.
- 21. H. Luo, B. Wang, Y. Li, T. Liu, W. You, D. Wang, *Electrochim. Acta*, 231 (2017) 479–486.
  - 22. E. Shangguan, F. Li, J. Li, Z. Chang, Q. Li, X.-Z. Yuan, H. Wang, *J. Power Sources*, 291 (2015) 29–39.
  - 23. E. Shangguan, S. Fu, C. Wu, X. Cai, J. Li, Z. Chang, Z. Wang, Q. Li, *Electrochim. Acta*, 301 (2019) 162–173.
  - 24. H. Weinrich, J. Come, H. Tempel, H. Kungl, R.A. Eichel, N. Balke, *Nano Energy*, 41 (2017) 706–716.
  - 25. S.D. Giri, A. Sarkar, *J. Electrochem. Soc.*, 163 (2016) H252–H259.
  - 26. Q. Wang, Y. Wang, *ACS Appl. Mater. Interfaces*, 8 (2016) 10334–10342.
  - 27. H. Weinrich, J. Come, H. Tempel, H. Kungl, R.-A. Eichel, N. Balke, *Nano Energy*, 41 (2017) 706–716.
  - 28. J. Li, G. LT, E. Shangguan, Y. MZ, M. Xu, D. Wang, C. ZR, L. QM, *Electrochim. Acta*, 240 (2017) 456–465.
  - 29. B.T. Hang, T. Watanabe, M. Egashira, I. Watanabe, S. Okada, J. ichi Yamaki, *J. Power Sources*, 155 (2006) 461–469.
  - 30. T.M.D. Dang, T.T.T. Le, E. Fribourg-Blanc, M.C. Dang, *Adv. Nat. Sci. Nanosci. Nanotechnol.*, 2 (2011) 1–6.
  - 31. R. Carta, S. Dernini, A.M. Polcaro, P.F. Ricci, G. Tola, *J. Electroanal. Chem. Interfacial Electrochem.*, 257 (1988) 257–268.